

Inferences on Flow at the Base of Earth's Mantle Based on Seismic Anisotropy

Mark Panning* and Barbara Romanowicz

process is irreversible. Sonication of any of the bundle, tubular, and even sheet-like assemblies results in irreversible dispersion of the rods under all conditions studied thus far, including elevated temperature (80°C, followed by slow cooling). The rate of sedimentation under these conditions effectively competes with the assembly process.

This study has introduced the concept of using polymer segments in nanorod structures to control their assembly into flat two-dimensional and curved three-dimensional structures. One can systematically make different architectures by controlling the composition of the rod structures and the ratio of the blocks of different materials that compose them. Insight into such assembly processes not only complements the work of others with mesoscopic and macroscopic assembly schemes (26, 27) but also is critical to understanding self-organization processes in unnatural systems and the exploitation of these versatile rod-like synthons in the fabrication of a new category of metal-polymer hybrid materials and, perhaps, devices.

References and Notes

1. Y. Xia *et al.*, *Adv. Mater.* **15**, 353 (2003).
2. S. Iijima, *Nature* **354**, 56 (1991).
3. H. Dai *et al.*, *Chem. Phys. Lett.* **260**, 471 (1996).
4. J. Kong, H. T. Soh, A. M. Cassell, C. F. Quate, H. Dai, *Nature* **395**, 878 (1998).
5. C. R. Martin, *Acc. Chem. Res.* **28**, 61 (1995).
6. S. R. Nicewarner-Pena *et al.*, *Science* **294**, 137 (2001).
7. X. Peng *et al.*, *Nature* **404**, 59 (2000).
8. G. R. Patzke, F. Krumeich, R. Nesper, *Angew. Chem. Int. Ed. Engl.* **41**, 2446 (2002).
9. X. Duan, Y. Huang, R. Agarwal, C. M. Lieber, *Nature* **421**, 241 (2003).
10. T. Rueckes *et al.*, *Science* **289**, 94 (2000).
11. C. R. Martin, *Science* **266**, 1961 (1994).
12. B. Nikoobakht, Z. L. Wang, M. A. El-Sayed, *J. Phys. Chem. B* **104**, 8635 (2000).
13. F. Kim, S. Kwan, J. Akana, P. Yang, *J. Am. Chem. Soc.* **123**, 4360 (2001).
14. E. Dujardin, L.-B. Hsin, C. R. C. Wang, S. Mann, *Chem. Commun.* **2001**, 1264 (2001).
15. N. I. Kovtyukhova, T. E. Mallouk, *Chem. Eur. J.* **8**, 4354 (2002).
16. N. R. Jana *et al.*, *J. Mater. Chem.* **12**, 2909 (2002).
17. K. K. Caswell, J. N. Wilson, U. H. F. Bunz, C. J. Murphy, *J. Am. Chem. Soc.* **125**, 13914 (2003).
18. G. A. Ozin, *Can. J. Chem.* **77**, 2001 (1999).
19. N. Hadjichristidis, S. Pispas, G. Floudas, *Block Copolymers: Synthetic Strategies, Physical Properties, and Applications* (Wiley-Interscience, Hoboken, NJ, 2002).
20. Materials and methods are available as supporting material on Science Online.
21. S. I. Stupp *et al.*, *Science* **276**, 384 (1997).
22. J. C. Love, A. R. Urbach, M. G. Prentiss, G. M. Whitesides, *J. Am. Chem. Soc.* **125**, 12696 (2003).
23. J. N. Israelachvili, *Intermolecular and Surface Forces* (Academic Press, San Diego, CA, 1992).
24. M. Steinhart *et al.*, *Science* **296**, 1997 (2002).
25. C. Levinthal, *J. Chim. Phys.* **65**, 44 (1968).
26. A. Terfort, N. Bowden, G. M. Whitesides, *Nature* **386**, 162 (1997).
27. M. J. MacLachlan, N. Coombs, G. A. Ozin, *Nature* **397**, 681 (1999).
28. C.A.M. acknowledges the U.S. Air Force Office of Scientific Research and NSF for supporting this research and G. Schatz for helpful discussions.

Supporting Online Material

www.sciencemag.org/cgi/content/full/303/5656/348/DC1
Materials and Methods

Figs. S1 to S3

4 November 2003; accepted 9 December 2003

We applied global waveform tomography to model radial anisotropy in the whole mantle. We found that in the last few hundred kilometers near the core-mantle boundary, horizontally polarized S -wave velocities (V_{SH}) are, on average, faster (by $\sim 1\%$) than vertically polarized S -wave velocities (V_{SV}), suggesting a large-scale predominance of horizontal shear. This confirms that the D'' region at the base of the mantle is also a mechanical boundary layer for mantle convection. A notable exception to this average signature can be found at the base of the two broad low-velocity regions under the Pacific Ocean and under Africa, often referred to as "superplumes," where the anisotropic pattern indicates the onset of vertical flow.

The core-mantle boundary (CMB) represents a thermal and a chemical boundary between Earth's solid silicate mantle and its liquid iron outer core. The corresponding boundary layer on the mantle side, often referred to as D'' , is thus the site of complex dynamic processes that may involve thermal and chemical heterogeneity at various scales [e.g., (1)]. Additionally, it has been suggested that this layer functions as a mechanical boundary layer for the convection of the overlying mantle, leading to intense deformation. Such deformation processes can lead to detectable seismic anisotropy, either through the alignment of anisotropic crystals in the strain field or through the fine layering of materials with contrasting elastic properties (2, 3).

The presence of anisotropy in D'' has been established in several regions, including under the central Pacific Ocean, north-eastern Asia, Alaska, and Central America, from the observation of seismic waves diffracting (S_{diff}) or reflecting (ScS) at the CMB (3–8). The limited areas of sampling, however, have made interpretation of these observations difficult. A more global picture of long-wavelength anisotropic D'' structure would clearly aid interpretation in terms of dynamic flow modeling as well as mineral physics.

With this in mind, we have adapted a global waveform tomography approach (9, 10) to develop a three-dimensional model of radial anisotropy in the whole mantle, using a large data set of three-component time-domain waveforms of surface and body waves (11). The model is parameterized in terms of isotropic V_S and the anisotropic ξ parameter ($\xi = V_{SH}^2/V_{SV}^2$), which

is directly related to radial anisotropy in S -wave velocity (12). With our data set and our broadband sensitivity kernels (9), which allow us to use both reflected and diffracted waves in D'' (fig. S1), we have enough coverage to invert for radially anisotropic structure in the whole mantle, as shown by resolution tests (13).

Our final model includes anisotropic S -wave velocity structure throughout the mantle. Two regions of strong "degree 0" radial anisotropy stand out in our model: the uppermost mantle and D'' (Fig. 1). In both regions, on average, V_{SH} is faster than V_{SV} . This can be interpreted, at least for the

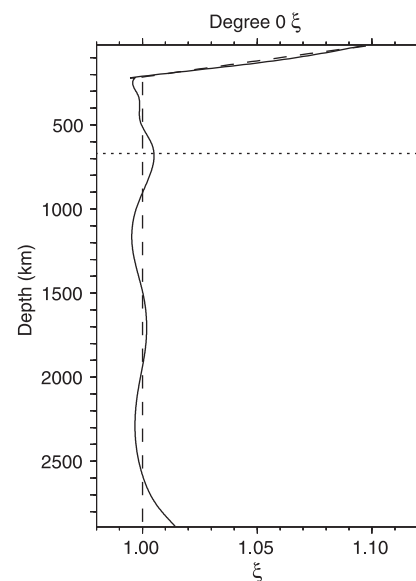


Fig. 1. Degree 0 model for ξ as a function of depth (solid line). The values for PREM (17) are shown by the dashed line. For reference, the 660-km discontinuity in the transition zone between the upper and lower mantle is shown (dotted line). Note the strong increase at the base of the mantle, similar but smaller in amplitude to that seen in the uppermost mantle.

Berkeley Seismological Laboratory, 215 McCone Hall, University of California, Berkeley, CA 94720, USA.

*To whom correspondence should be addressed. E-mail: mpanning@seismo.berkeley.edu

REPORTS

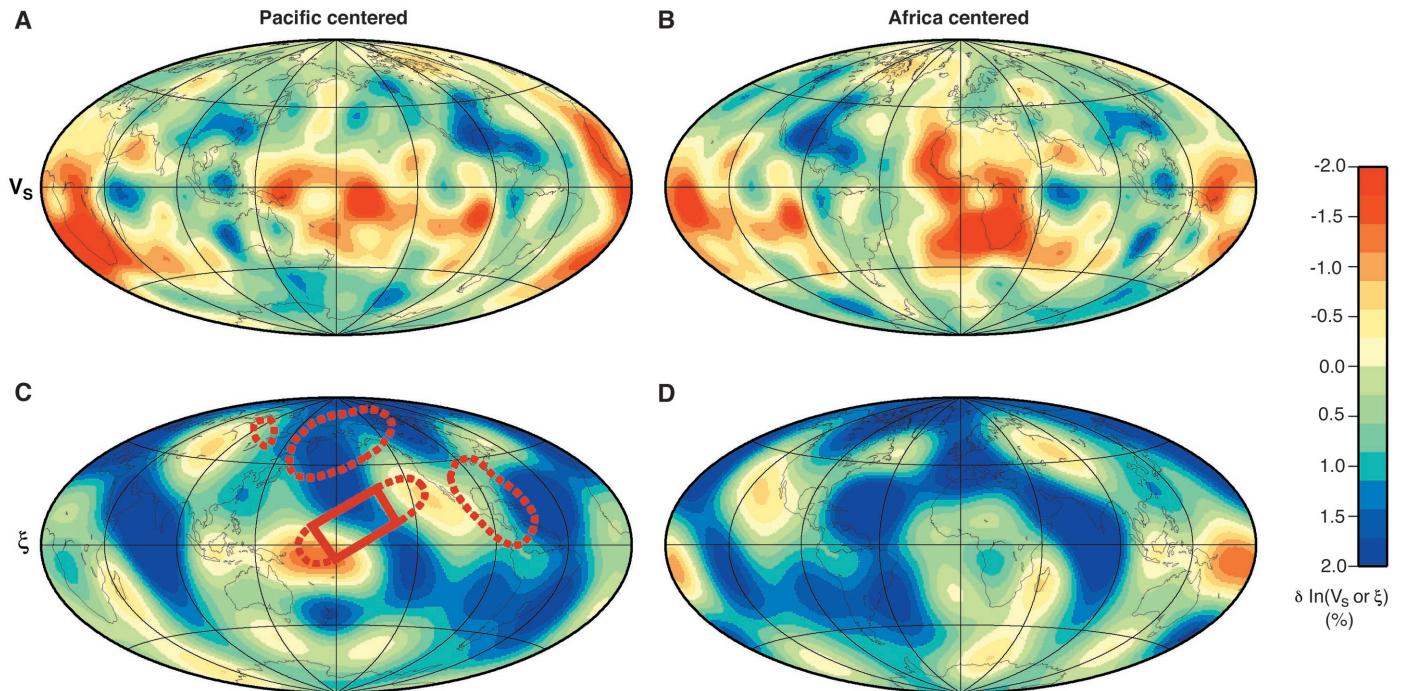


Fig. 2. Distribution of $\delta \ln(V_s)$ (A and B) and $\delta \ln(\xi)$ (C and D) at a depth of 2800 km. Maps are shown centered under the Pacific (A and C) and Africa (B and D). Also shown in C are the regions of D'' sampled by previous regional studies. Dotted areas indicate observations of $V_{SH} > V_{SV}$; the box in the central Pacific denotes a region with highly variable

observations including $V_{SV} > V_{SH}$ [adapted from (5)]. The shift of the zone of $\delta \ln(\xi) > 0$ to the east of Central America in our model may be a result of the long-wavelength parameterization in our model. However, recent studies have documented that D'' in Central America is the site of strong lateral gradients of structure (26), so this transition may be real.

upper mantle, as indicating the presence of strong horizontal shear, consistent with previous work (14–17). The isotropic part of the model (Fig. 2, A and B) is consistent with earlier tomographic models of shear velocity in this depth range (10, 18, 19) and is characterized by a strong degree 2 component representing a fast ring surrounding two low-velocity features (often called superplumes) centered beneath the central Pacific Ocean and Africa. The strong degree 0 component in ξ [$\delta \ln(\xi) > 0$] dominates the map in D'' (Fig. 2, C and D). The regions that differ most strongly from this average structure correlate well with the locations of the two superplumes, with reduced values of $\delta \ln(\xi)$ under the central Pacific Ocean, Africa, and the south Atlantic Ocean, including patches with negative values ($V_{SV} > V_{SH}$). Another two large patches of reduced $\delta \ln(\xi)$ are seen just west of North America and under central Eurasia. These patches also are related to slow isotropic velocities, although these regions of depressed velocities are much smaller than the two superplumes.

Although the finer scale features of our model may not be resolvable, and although observations in regions with high gradients will display some differences due to the long-wavelength parameterization of our model (20), the long-wavelength anisotropic features imaged in our model generally agree with more localized studies of D''

anisotropy (Fig. 2C). Specifically, earlier studies imaged areas with positive $\delta \ln(\xi)$ beneath Central America and Alaska (5, 8) as well as northeastern Asia (7). The central Pacific regional results are more variable, with some areas showing negative $\delta \ln(\xi)$ (3, 5, 8).

The dominant $V_{SH} > V_{SV}$ found as one approaches the CMB suggests that the anisotropy observed in D'' is related to the dominant horizontal flow in a mechanical boundary layer, analogous to the larger signal observed in the uppermost 200 km of the mantle and factored into the construction of the Preliminary Reference Earth Model (PREM) (17). As one approaches regional regions of upwelling, the direction of flow changes and results in a different signature of anisotropy, as manifested in our study under the central Pacific and Africa. Anisotropy in these regions bordering the large-scale upwellings may be much more complex and include tilting of the axis of symmetry, which we assume to be vertical in our modeling. This would result in azimuthal anisotropy, which we do not attempt to model here.

Whether the globally observed anisotropy is due to lattice-preferred orientation (LPO) (2, 21) or the alignment of materials with differing elastic properties through shape-preferred orientation (SPO) (3) must await direct measurements of how lowermost mantle materials will develop

LPO anisotropy at the corresponding temperature and pressure conditions. Arguments for weak anisotropy in perovskite [(Mg,Fe)SiO₃] and strong positive ξ in periclase (MgO) (2) as well as for negative ξ in both perovskite and periclase (22) have been advanced with the use of theoretical methods. Some studies have shown that high strain in subducting slabs approaching the CMB might be able to sustain conditions necessary for producing LPO structure across broad regions of D'' (21). This model also shows that although the major axes of the strain ellipses are horizontal under the downgoing slabs, the material can be rotated to vertical as it approaches upwellings, possibly explaining the observed change in anisotropy below the superplumes in our model. Different SPO hypotheses have been advanced as well, mostly relating to horizontal layering or inclusion of variously shaped pockets of contrasting material. Candidates for the differing elastic properties include reaction products from core-mantle interaction (23) and melted former basalt in a slab graveyard (3, 5). In general, these SPO models lead to positive ξ , although if there is tilting of the pockets of differing material under deformation, considerable azimuthal variation in velocities could be observed (2).

Whatever the cause, our results clearly show that the dynamics of D'' correspond with what would be expected in a boundary

layer dominated by horizontal flow and emphasize the unique character of the two superplume regions, for which we bring additional evidence of large-scale upwelling. Although measurements of deformation at the pressures and temperatures corresponding to the CMB region are not yet available, our results suggest that similar relationships between anisotropic signature and flow prevail in the uppermost and lowermost mantle.

References and Notes

1. T. Lay, Q. Williams, E. J. Garnero, *Nature* **392**, 461 (1998).
2. S.-I. Karato, *Earth Planets Space* **50**, 1019 (1998).
3. J.-M. Kendall, P. G. Silver, *Nature* **381**, 409 (1996).
4. L. P. Vinnik, V. Farra, B. Romanowicz, *Geophys. Res. Lett.* **16**, 519 (1989).
5. T. Lay, Q. Williams, E. J. Garnero, L. Kellogg, M. Wyssession, in *The Core-Mantle Boundary Region*, M. Gurnis, M. E. Wyssession, E. Knittle, B. A. Buffett, Eds. (American Geophysical Union, Washington, DC, 1998), pp. 219–318.
6. S. A. Russell, T. Lay, E. J. Garnero, *J. Geophys. Res.* **104**, 13183 (1999).
7. C. Thomas, J.-M. Kendall, *Geophys. J. Int.* **151**, 296 (2002).
8. M. S. Fouch, K. M. Fischer, M. E. Wyssession, *Earth Planet. Sci. Lett.* **190**, 167 (2001).
9. X. D. Li, B. Romanowicz, *Geophys. J. Int.* **121**, 695 (1995).
10. C. Mégnin, B. Romanowicz, *Geophys. J. Int.* **143**, 709 (2000).
11. Our data set consists of three-component long-period seismograms (minimum period of 60 s for surface waves and 32 s for body waves) inverted in the time domain in the framework of nonlinear asymptotic coupling theory (9). In this normal-mode perturbation-based approach, we calculate two-dimensional great-circle sensitivity kernels that account for the distribution of sensitivity along and in the vicinity of the ray when using finite-frequency waveform data. Additionally, this approach allows us to use diffracted waves as well as simultaneously arriving phases, which is not possible when using ray theory– and travel time–based approaches (fig. S1 and SOM text).
12. Our model is parameterized in terms of radial anisotropy, which is usually described by density ρ , and five elastic coefficients ($A = \rho V_{P,H}^2$, $C = \rho V_{P,V}^2$, $L = \rho V_{S,H}^2$, $N = \rho V_{S,V}^2$, and F). We chose to describe this equivalently in terms of the isotropic P and S velocities [$V_{P,iso}^2 = 1/5(V_{P,V}^2 + 4V_{P,H}^2)$ and $V_{S,iso}^2 = 1/3(V_{S,H}^2 + 2V_{S,V}^2)$] and three anisotropic parameters [$\xi = N/L$, $\phi = C/A$, and $\eta = F/(A - 2L)$]. The isotropic velocities are derived from the Voigt average isotropic elastic properties (24). These can be expressed as $\rho V_P^2 = (1/15)[3C + (8 + 4\eta)A + 8(1 - \eta)L]$ and $\rho V_S^2 = (1/15)[C + (1 - 2\eta)A + (6 + 4\eta)L + 5N]$. Because in this approach we assume anisotropy to be small, we can simplify the kernel calculation by using $\eta \approx 1$ and $A \approx C$ to reduce the Voigt average expressions to the ones used above. To reduce the number of free parameters in the inversion, we assume the following scaling relationships: $\delta \ln(V_{P,iso}) = 0.5 \delta \ln(V_{S,iso})$, $\delta \ln(\eta) = -2.5 \delta \ln(\xi)$, $\delta \ln(\phi) = -1.5 \delta \ln(\xi)$, and $\delta \ln(\rho) = 0.3 \delta \ln(V_{S,iso})$. Scaling relations for the anisotropic parameters have been determined in the laboratory only for conditions down to 500 km (25), so we also performed a lower resolution inversion where ξ , ϕ , and η were allowed to vary independently. The structure in ξ changed very little, and analysis of the resolution matrix indicated that ξ was indeed the best resolved of the three parameters, and tradeoffs were not too strong (fig. S2). The model was parameterized with 16 splines radially, and by spherical harmonics horizontally up to degree 16 for $V_{S,iso}$ and degree 8 for ξ .
13. We performed several tests using the resolution matrix calculated for an inversion up to degree 16 in both V_S and ξ . Tests with a random input model with a white wavelength spectrum indicate that we are capable of correctly resolving the long-wavelength ξ structure with some resolution at

- shorter wavelengths in the upper and lowermost mantle (fig. S3), but not in the bulk of the lower mantle. On this basis, we limited our inversion to degree 8 in ξ . Statistical tests also demonstrate improvement in fit significant at a 95% confidence level for the CMB-sensitive portion of the data set for the model with ξ structure in the lowermost 400 km of the mantle compared to an isotropic model (SOM text).
14. J.-P. Montagner, T. Tanimoto, *J. Geophys. Res.* **96**, 20337 (1991).
15. G. Ekström, A. M. Dziewonski, *Nature* **394**, 168 (1997).
16. Y. Gung, M. Panning, B. Romanowicz, *Nature* **422**, 707 (2003).
17. A. M. Dziewonski, D. L. Anderson, *Phys. Earth Planet. Inter.* **25**, 297 (1981).
18. G. Masters, S. Johnson, G. Laske, B. Bolton, *Philos. Trans. R. Soc. London Ser. A* **354**, 1385 (1996).
19. Y. J. Gu, A. M. Dziewonski, W. Su, G. Ekström, *J. Geophys. Res.* **106**, 11169 (2001).
20. As shown by resolution tests, only the long-wavelength features of our model are well constrained (13). Moreover, we have ignored azimuthal anisotropy, which may influence the details of our model, although radial an-

- isotropy has been shown to adequately describe the data in many of the regional studies (5).
21. A. K. McNamara, P. E. van Keken, S.-I. Karato, *Nature* **416**, 310 (2002).
22. L. Stixrude, in *The Core-Mantle Boundary Region*, M. Gurnis, M. E. Wyssession, E. Knittle, B. A. Buffett, Eds. (American Geophysical Union, Washington, DC, 1998), pp. 83–96.
23. E. Knittle, R. Jeanloz, *Science* **251**, 1438 (1991).
24. V. Babuska, M. Cara, *Seismic Anisotropy in the Earth* (Kluwer Academic, Boston, 1991).
25. J.-P. Montagner, D. L. Anderson, *Phys. Earth Planet. Inter.* **54**, 82 (1989).
26. M. E. Wyssession, K. M. Fischer, G. I. Al-eqabi, P. J. Shore, I. Gurari, *Geophys. Res. Lett.* **28**, 867 (2001).
27. This is contribution 03-10 of the Berkeley Seismological Laboratory. Supported by NSF grant EAR-9902777.

Supporting Online Material
www.sciencemag.org/cgi/content/full/303/5656/351/DC1
 SOM Text
 Figs. S1 to S7

15 September 2003; accepted 3 December 2003

Siberian Peatlands a Net Carbon Sink and Global Methane Source Since the Early Holocene

L. C. Smith,^{1,2*} G. M. MacDonald,^{1,3*} A. A. Velichko,⁴
 D. W. Beilman,¹ O. K. Borisova,⁴ K. E. Frey,¹ K. V. Kremenetski,^{1,4}
 Y. Sheng¹

Interpolar methane gradient (IPG) data from ice cores suggest the “switching on” of a major Northern Hemisphere methane source in the early Holocene. Extensive data from Russia’s West Siberian Lowland show (i) explosive, widespread peatland establishment between 11.5 and 9 thousand years ago, predating comparable development in North America and synchronous with increased atmospheric methane concentrations and IPGs, (ii) larger carbon stocks than previously thought (70.2 Petagrams, up to ~26% of all terrestrial carbon accumulated since the Last Glacial Maximum), and (iii) little evidence for catastrophic oxidation, suggesting the region represents a long-term carbon dioxide sink and global methane source since the early Holocene.

Ice-core records of atmospheric methane concentration show dramatic peaks in the early Holocene, drawing considerable debate as to their source (1). Expansion of tropical wetlands has emerged as a popular hypothesis (2–5), in part because high-latitude peatlands were not well developed in North America by ~11,000 calendar years ago (11 ka), a period of peak methane concentration. However, the timing and volume of peatland growth in Russia, which contains perhaps half of the world’s peat, is virtually unknown. Published esti-

mates of carbon storage in high-latitude peatlands are poorly constrained but large (180 to 455 Pg C) (6), representing up to ~1/3 of the global soil carbon pool (1395 Pg C) (7). Most are known to have formed since the Last Glacial Maximum and thus represent a major terrestrial carbon sink during the Holocene (8). However, the true magnitude and timing of this sink is poorly known because of insufficient data on peatland distribution through time (9), depth, area, age, and carbon content (6, 10). These uncertainties make it difficult to infer the influence of northern peatlands on Holocene greenhouse gas concentrations and to predict the amount of sequestered carbon that could potentially be mobilized under a warmer Arctic climate through water table lowering, peat oxidation, and CO₂ outgassing (6, 11, 12); biosphere uptake (11, 12); or increased dissolved organic carbon efflux to rivers (13).

¹Department of Geography, ²Department of Earth and Space Sciences, ³Department of Organismic Biology, Ecology and Evolution, University of California, Los Angeles, CA 90095–1524, USA. ⁴Russian Academy of Sciences, Moscow 109017, Russia.

*To whom correspondence should be addressed. E-mail: lsmith@geog.ucla.edu (L.C.S.); macdonal@geog.ucla.edu (G.M.M.)